Digital Discovery

ROYAL SOCIETY OF CHEMISTRY

PAPER

View Article Online
View Journal | View Issue

Cite this: *Digital Discovery*, 2026, **5**, 453

Deep learning based SEM image analysis for predicting ionic conductivity in $LiZr_2(PO_4)_3$-based solid electrolytes

Kento Murakami,[a] Yudai Yamaguchi,[a] Yo Kato,[a] Kazuki Ishikawa,[b] Naoto Tanibata,[a] Hayami Takeda,*[a] Masanobu Nakayama*[a] and Masayuki Karasuyama[b]

Lithium-ion-conductive oxide materials have attracted considerable attention as solid electrolytes for all-solid-state batteries. In particular, $LiZr_2(PO_4)_3$-related compounds are promising for high-energy-density devices using metallic lithium anodes, but further enhancement of their ionic conductivity is requested. In general, Li-ion conductivity is influenced by mechanisms operating on two distinct length scales. At the atomic scale, point defects and the associated migration barriers within the crystal lattice are critical, whereas at the micrometre scale, porosity and grain-boundary characteristics that develop during sintering become the dominant factors. These coupled effects make systematic optimization of conductivity difficult. In paticular, microstructural analysis has often relied on researchers' intuitive interpretation of scanning electron microscopy (SEM) images. Here, we apply a convolutional neural network (CNN), a deep-learning approach that has seen rapid advances in image analysis, to SEM images of $LiZr_2(PO_4)_3$-based electrolytes. By combining image-derived features with conventional vector descriptors (composition, sintering parameters, *etc.*), our regression model achieved an R^2 of 0.871. Furthermore, visual-interpretability analysis of the trained CNN revealed that grain-boundary regions were highlighted as low-conductivity areas. These findings demonstrate that deep-learning-based SEM analysis enables automated, quantitative evaluation of ionic conductivity and offers a powerful tool for accelerating the development of solid electrolyte materials.

Received 27th May 2025
Accepted 12th December 2025

DOI: 10.1039/d5dd00232j

rsc.li/digitaldiscovery

Introduction

Fast lithium-ion conducting oxides serve as solid electrolytes for all-solid-state lithium secondary batteries. They are particularly anticipated to resolve the safety concerns linked to conventional flammable liquid electrolytes, especially in large-scale applications like electric vehicles.[1–5] Moreover, solid electrolytes hold promise as they do not react with lithium metal and can inhibit dendrite growth, facilitating the use of lithium metal anodes and thereby significantly enhancing battery capacity.[6]

Oxide-based lithium-ion conductors are considered advantageous due to their nonflammability, chemical stability, and mechanical strength.

Representative oxide-based lithium-ion conductors with high ionic conductivity include perovskite-type $Li_{0.5}La_{0.5}TiO_3$,[7] garnet-type $Li_7La_3Zr_2O_{12}$ (LLZ),[8] and NASICON-type compounds such as $Li_{1.5}Al_{0.5}Ge_{1.5}P_2O_{12}$,[9] $Li_{1.3}Al_{0.3}Ti_{1.7}(PO_4)_3$ (LATP),[10] and $LiZr_2(PO_4)_3$.[11] Among these, LLZ and $LiZr_2(PO_4)_3$ are particularly notable because they do not react with metallic lithium, making them promising candidates for high-energy-density all-solid-state batteries with lithium metal anodes. However, LLZ is known to be sensitive to experimental conditions, such as its high reactivity with moisture and CO_2 in air, and variations in conductivity depending on the incorporation of Al from crucibles during synthesis.[12]

Among them, NASICON-type $LiZr_2(PO_4)_3$ materials have attracted attention as they combine high lithium-ion conductivity with durability against metallic lithium. In fact, Li *et al.* successfully fabricated a high-capacity all-solid-state battery using lithium metal, composed of $Li/LiZr_2(PO_4)_3/LiFePO_4$, and reported stable cycle performance.[13]

To date, many attempts have been made to improve the conductivity of $LiZr_2(PO_4)_3$ by controlling its composition through doping with different elements.[14–25] In addition, when using oxide materials as solid electrolytes, it is essential to obtain dense sintered bodies in terms of mechanical durability and the reduction of grain boundary resistance. The control of oxide sintering depends on heating temperature, atmosphere, time, and raw powder characteristics. Generally, increasing the heating temperature enhances the sintering density. However, in the case of $LiZr_2(PO_4)_3$, components such as Li and P often volatilize at high temperatures, making it necessary to optimize the heating conditions.[26,27]

[a]*Department of Advanced Ceramics, Nagoya Institute of Technology, Gokiso, Showa, Nagoya, Aichi 466-8555, Japan. E-mail: takeda.hayami@nitech.ac.jp; masanobu@nitech.ac.jp*

[b]*Department of Computer Science, Nagoya Institute of Technology, Gokiso, Showa, Nagoya, Aichi 466-8555, Japan*

We have attempted to maximize lithium-ion conductivity in $Li_{1+2x+y}Ca_xZr_{2-x}Si_yP_{3-y}O_{12}$ (hereinafter referred to as LCZSP) materials, in which Ca and Si are substituted, by controlling the composition of Ca and Si[28] or the heating conditions.[26,29] For example, in composition control, the amount of Ca doping was found to influence microstructure of sintered body, while Si doping was associated with the formation of the α-phase (high ionic conductivity) and β-phase (low ionic conductivity), significantly affecting lithium-ion conductivity (from 2.7×10^{-5} to 2.3×10^{-8} S cm^{-1} at 30 °C).[27,28]

Furthermore, even with the same composition, we found that systematically varying the first and second heating temperatures resulted in significant changes in lithium-ion conductivity over two orders of magnitude (from 3.3×10^{-5} to 6.4×10^{-7} S cm^{-1} at 30 °C).[26] It was also revealed that the optimal heating temperature lies in the middle of the specified temperature range, suggesting a trade-off relationship likely due to sintering density and component volatilization as mentioned above. These findings clearly indicate that optimizing the composition and processing conditions is crucial in the development of solid electrolyte materials.

Optimization of composition and processing has traditionally relied on a trial-and-error approach based on the knowledge and experience of researchers and engineers. However, in recent years, materials development utilizing Materials Informatics (MI) has been explored. MI aims to predict physical properties such as activation energy using machine learning, and by applying information science to materials development, it is expected to accelerate the discovery of new functional materials.[30–32] We have demonstrated efficient determination of the optimized temperature and composition by applying Bayesian optimization to LCZSP materials.[26–28] However, one challenge with above mentioned Bayesian optimization is that it employs black-box functions, such as Gaussian process regression, which often fails to provide systematic knowledge on factors affecting Li ion conductivity. Traditionally, various analytical techniques have been used to understand the mechanisms underlying material functionality. For inorganic crystalline compounds, commonly used methods include X-ray Diffraction (XRD) for analyzing crystal phases, Scanning Electron Microscope (SEM) for observing microstructure, and X-ray Photoelectron Spectroscopy (XPS) for elemental analysis and chemical bonding states of surfaces. Recently, we evaluated the relationship between XRD profiles obtained from LCZSP materials sintered at various temperatures and the solid electrolyte properties (activation energy for lithium-ion conduction) using deep learning with an attention mechanism.[33] As a result, it was suggested that the activation energy can be predicted from XRD profiles and is mainly influenced by the resulting crystal phases (α-phase, β-phase, and impurity phases). On the other hand, while XRD is sensitive to crystal structures derived from composition and atomic arrangements, it is not suitable for analyzing microscale information such as particle morphology and sintering microstructures. SEM images are effective tools for analyzing micrometer-scale information, and indeed, studies have been reported in which such images are directly analyzed using deep learning techniques. For example, Kondo *et al.*[34] developed a model that predicts oxide ionic conductivity in yttria-stabilized zirconia by training a modified VGG16 convolutional neural network (CNN)[35] on microscopic images of ceramic microstructures. Furthermore, by visualizing the intermediate features in the CNN architecture, they specified microstructural features in SEM images affecting measured ionic conductivity positively or negatively. More recently, deep learning has also been used to elucidate the relationships between microstructures and properties such as mechanical strength and thermal conductivity in sintered silicon nitride ceramics (a heat-resistant structural material),[36] and between sintered structures and ionic conductivity in lithium-ion conductive materials.

In this study, we acquired 130 SEM image data for a total of 52 sintered LCZSP specimens, each with different compositions and sintering conditions, for which ionic conductivity had been measured previously, and then used a CNN to predict their conductivities. We placed particular emphasis on how microstructure affects ion transport, and sought to deepen our understanding of LCZSP ionic conduction by visualizing which regions of the SEM images exert positive or negative influence on conductivity.[37]

Method

Dataset & evaluation

All samples used in this study, including those reported in our previous publications, were synthesized and characterized by the authors. In detail, the dataset used for the LZP materials consisted of 52 LCZSP samples, where Zr was partially substituted by Ca and P was partially substituted by Si.[26,28,29] The samples varied in Si and Ca doping levels (x, y) in $Li_{1+2x+y}Ca_xZr_{2-x}Si_yP_{3-y}O_{12}$ (LCZSP) and the temperatures of both the first and second heating processes. The ranges of x and y were 0.05–0.4 and 0.05–0.15, respectively. The 1st and 2nd heating temperatures ranged from 900–1300 °C and 1100–1350 °C, respectively. The first heating was a pre-heating step intended to synthesize precursors while preventing compositional changes due to the evaporation of low-melting or volatile components. This was followed by intermittent grinding and a second heating, which aimed to promote diffusion among elements for phase formation and densification. The ionic conductivity at 30 °C, derived from the total resistance of grains and grain boundaries measured by impedance spectroscopy, varied from $10^{-6.8}$ to $10^{-4.5}$ S cm^{-1}. Fig. 1 illustrates how the measured ionic conductivity varied with composition (x, y) and heating temperatures, and details of the dataset are provided in Table S1 (SI) and in the associated repository.[38] To prepare input for the CNN, SEM images of the sintered pellet surfaces of 52 LCZSP materials [25, 26] were acquired. All SEM images were taken using a JSM-6360LV (JEOL, Japan) at an accelerating voltage of 20 kV and 1000 times magnification. To expand the dataset, 3 distinct surface locations were photographed per material, resulting in a total dataset of 130 SEM images. Fig. 2 shows representative SEM images. As seen in Fig. 2(a), samples sintered at lower temperatures tended to exhibit columnar particles, likely indicating the formation of the β-phase, which has lower ionic conductivity.[39] Depending on the composition

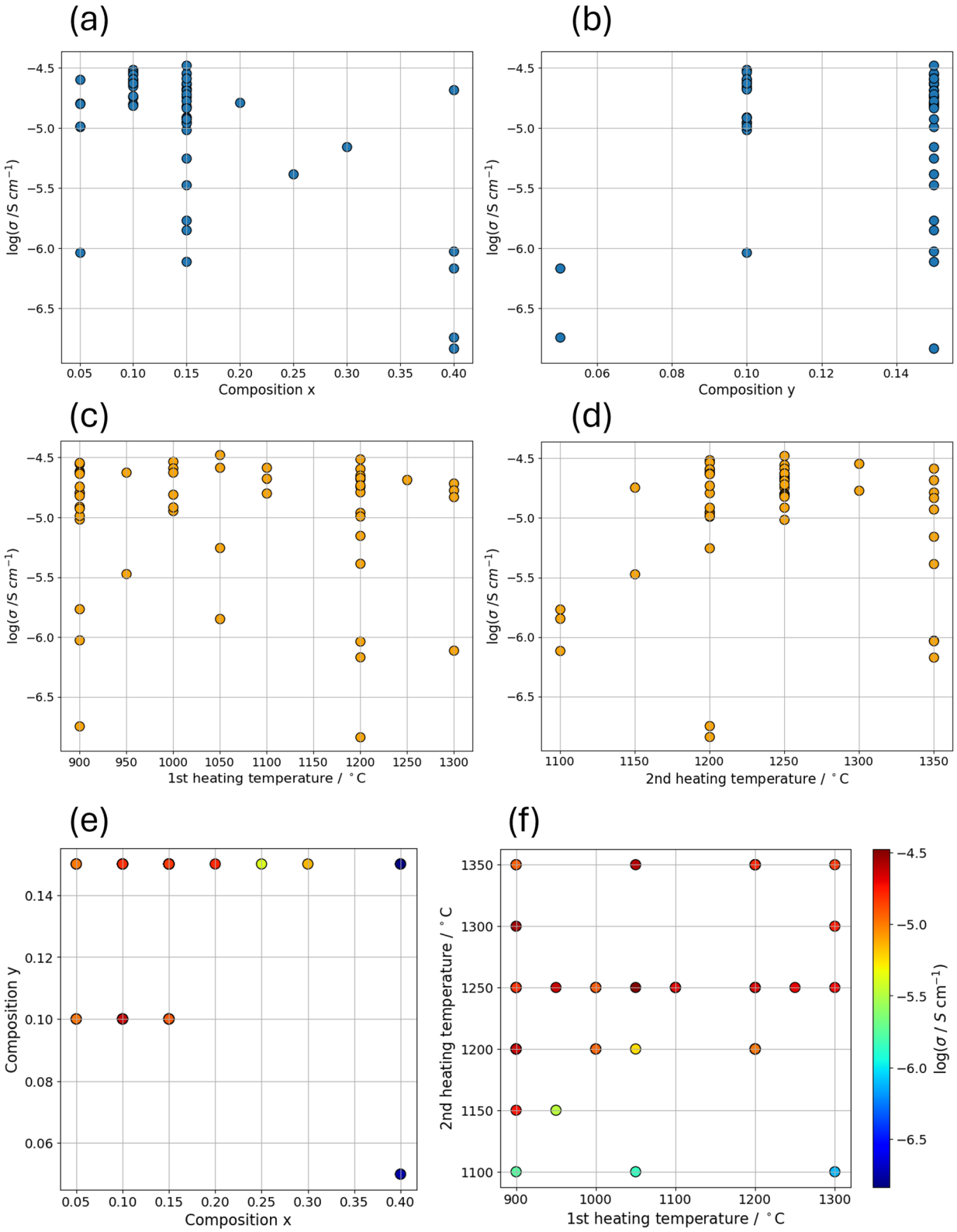

Fig. 1 Relationship between ionic conductivity and composition and heating temperature in $Li_{1+2x+y}Ca_xZr_{2-x}Si_yP_{3-y}O_{12}$ (52 samples). Panels (a)–(d) show the logarithm of the measured ionic conductivity at 30 °C as functions of the composition parameters x and y, and the first and second heating temperatures, respectively. Panels (e) and (f) display the sampling points in the (x, y) composition space and in the first and second heating temperature space, respectively. The color of each point represents the logarithm of the ionic conductivity at 30 °C, as indicated by the color bar on the right.

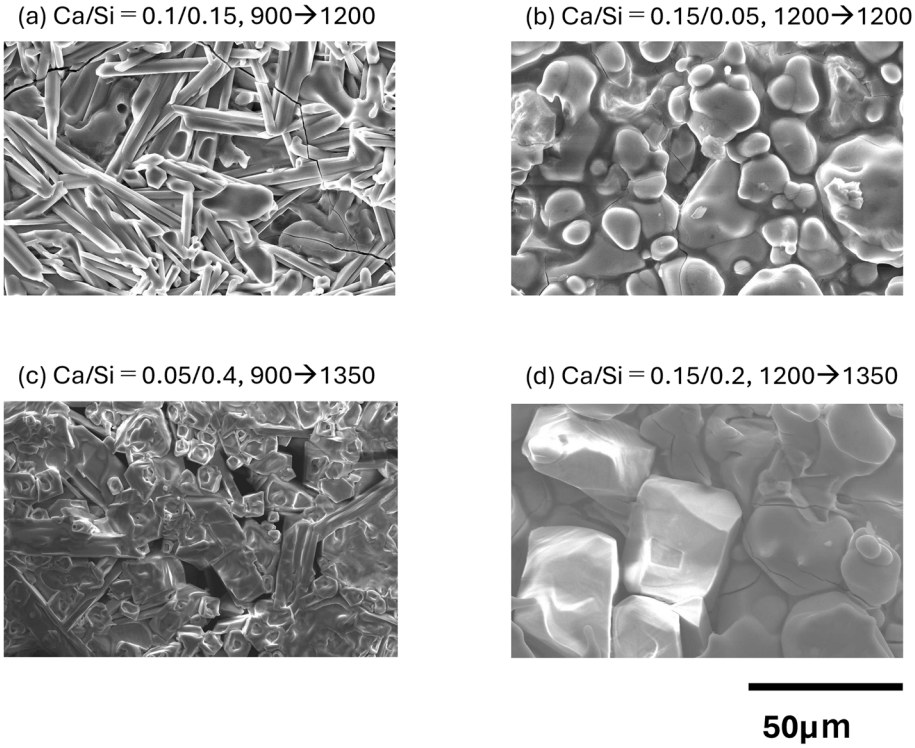

Fig. 2 SEM image of the surface of a representative $Li_{1+x+2y}Ca_yZr_{2-y}Si_xP_{3-x}O_{12}$ sintered body. The Ca/Si labels indicate the composition y/x ratio. The two numbers connected by an arrow indicate the temperatures of the 1st and 2nd heating (units: °C).

and sintering conditions, some samples exhibited intra-particle voids as seen in Fig. 2(c), while others showed significant particle growth as seen in Fig. 2(d). For these images, during training and verification, we randomly cropped (512 × 512 pixels) after flipping them horizontally and vertically with a probability of 50%, and prepared a total of 130 image data samples, one three for each sample. Center cropping (512 × 512 pixels) was used during testing (see validation method described later). These augmentations are effective for suppressing overfitting and improving model performance by diversifying the training data. The target variable was the ionic conductivity at 30 °C, and due to the wide distribution across several orders of magnitude, logarithmic values were used. For each sintered pellet, one-three SEM images were taken at different surface locations to enlarge the dataset. All three images from the same pellet share the same measured ionic conductivity value. (Number of SEM images per sample is listed in the SI Datasets.)

For training the CNN model, we employed leave-one-out cross-validation, which is suitable for small datasets. Since each material had three images, all three were used as the test set for that material, while the remaining 153 images were used for training and validation (Fig. 1). Four-fold cross-validation ($k = 4$) was performed on the training data, and the hyperparameters that yielded the minimum loss were adopted. Details of these hyperparameters are listed in Table S2. The four models obtained through k-fold cross-validation were used to predict the test data, and their average was taken as the final prediction. Mean Squared Error (MSE) was used as the loss function for training and validation, while Root Mean Squared Error (RMSE) and the R^2 score were used as evaluation metrics for the test data. For training the CNN model, we employed leave-one-out cross-validation at the sample level, which is suitable for small datasets. Each material was associated with 1–3 SEM images, and all of the images belonging to the held-out sample were used together as the test set. The remaining images (from the other 51 samples, totaling 127–155 images depending on the test case) were used for training and validation (Fig. 1). This procedure ensures that no data leakage occurs between training and test sets, as different images from the same sample were never split across them.

Four-fold cross-validation ($k = 4$) was then performed on the training portion, and the hyperparameters that yielded the minimum loss were adopted. Details of these hyperparameters are listed in Table S2. The four models obtained through k-fold cross-validation were used to predict the test data, and their average was taken as the final prediction. Mean Squared Error (MSE) was used as the loss function for training and validation, while Root Mean Squared Error (RMSE) and the R^2 score were used as evaluation metrics for the test data.

Machine learning

Table 1 presents a summary of the neural network architectures used in this study. We conducted evaluation experiments on a total of four architectures, including the pre-packaged Efficient Net[40] and a model based on that of Kondo *et al.*[34] Efficient Net is a deep learning model pretrained on the ImageNet dataset,[41] and it is currently widely used due to its higher

Table 1 List of CNN architectures employed table

Model name	Mode	Figure
Efficient Net-B3	Transfer	—
Baseline	Original	Fig. S1
Baseline with descriptors	Original	Fig. S2
Baseline with Attention	Original	Fig. S3

accuracy compared to traditional CNNs, despite having fewer parameters. In this study, transfer learning was performed using pretrained parameters. Due to computational constraints, we adopted EfficientNet-B3, which is considered medium-sized within the EfficientNet series.

Among the remaining architectures, the "Baseline" model represents the simplest structure, and the other two are modifications of this "Baseline" model. The detailed structure of the "Baseline" model is shown in Table 2. In the "Baseline with descriptors" model, we focused on the Global Average Pooling (GAP) layer and observed changes in regression accuracy by concatenating additional material-derived descriptors to the one-dimensional feature vector. The "Baseline with Attention" model introduces an attention mask into the intermediate convolutional layers.[33,42–44] Specifically, a single image is generated from the feature maps using a 1×1 convolution,[45–48] and a Sigmoid function is applied to this image to transform it into an attention mask (attention score). This mask is then element-wise multiplied (Hadamard product) with each original feature map to produce a set of weighted feature maps, which are passed on to the next layer. The attention mask highlights the regions that should be focused on, thus enhancing the effect of feature extraction through convolution.

The schematic figure of the "Baseline," "Baseline with descriptors," and "Baseline with Attention" architectures are shown in Fig. S1–S3, respectively. Also codes are available in the associated repository.[49] In addition, to address the concern that the network design might be overly simplistic, we conducted supplementary experiments by increasing the depth of the "Baseline" model ((1) doubling convolutional layers, (2) doubling fully connected layers, and (3) doubling both). The results, summarized in SI Table S3, show that these deeper variants did not yield any significant improvement in RMSE compared to the original Baseline model. This confirms that the adopted network depth is already appropriate for the dataset size, and deeper architectures only increased the risk of overfitting without enhancing predictive accuracy.

Results & discussion

Regression analysis

For all evaluations, cropped SEM images resized to 512×512 pixels were used as input data. First, the results of predictions on the test data using a model trained *via* cross-validation with the Efficient Net-B3 derived model are shown in Fig. 3(a). As previously mentioned, three images of the same material were used as the test set, and the remaining data were used for training. The diagnostic plot in Fig. 2 shows the average predicted values for the three test images. The coefficient of determination (R^2) for the test data was approximately 0.63. While this indicates that qualitative classification between high and low ionic conductivity materials was achieved to some extent, it was not sufficient for quantitative evaluation. Particularly in the low ionic conductivity region, where data points were relatively sparse, significant prediction errors were observed. This is believed to be due to insufficient training caused by the limited amount of available data. We further examined the variability of predicted values across multiple SEM images of the same sample (see Fig. S5). The results showed that the variability was somewhat larger for low-conductivity samples; however, this is mainly due to the logarithmic scale, which amplifies small numerical deviations. Importantly, no outlier-like behavior was observed among images of the same sample, indicating that increasing the number of SEM images per sample would likely provide only limited benefit in accuracy while increasing experimental and computational costs. Fig. 3(b) shows the diagnostic plot for test data using the "Baseline" architecture. It is clear that the accuracy is lower compared to the Efficient Net-B3 derived model. The "Baseline" model is the simplest CNN architecture used in this study, and it has significantly fewer trainable parameters (weights) compared to Efficient Net-B3. Nevertheless, the prediction trend was similar to that of Efficient Net, with higher prediction accuracy for images corresponding to high ionic conductivity (where more data were available), and lower accuracy for low conductivity images (with less data). To improve prediction accuracy while keeping the descriptor set

Table 2 A specific structure of "Baseline" architecture

Type	Input	Kernel	Stride	Pad	Output
Input	$512 \times 512 \times 1$	N/A	N/A	N/A	$512 \times 512 \times 1$
Convolution	$512 \times 512 \times 1$	3×3	1	1	$512 \times 512 \times 16$
Convolution	$512 \times 512 \times 16$	3×3	1	1	$512 \times 512 \times 16$
Max pooling	$512 \times 512 \times 16$	2×2	2	0	$256 \times 256 \times 16$
Convolution	$256 \times 256 \times 16$	3×3	1	1	$256 \times 256 \times 32$
Convolution	$256 \times 256 \times 32$	3×3	1	1	$256 \times 256 \times 32$
Max pooling	$256 \times 256 \times 32$	2×2	2	0	$128 \times 128 \times 32$
Convolution	$128 \times 128 \times 32$	3×3	1	1	$128 \times 128 \times 64$
Convolution	$128 \times 128 \times 64$	3×3	1	1	$128 \times 128 \times 64$
Global average pooling	$128 \times 128 \times 64$	128×128	1	0	$1 \times 1 \times 64$
Fully connected	$1 \times 1 \times 64$	1×1	1	0	$1 \times 1 \times 1$

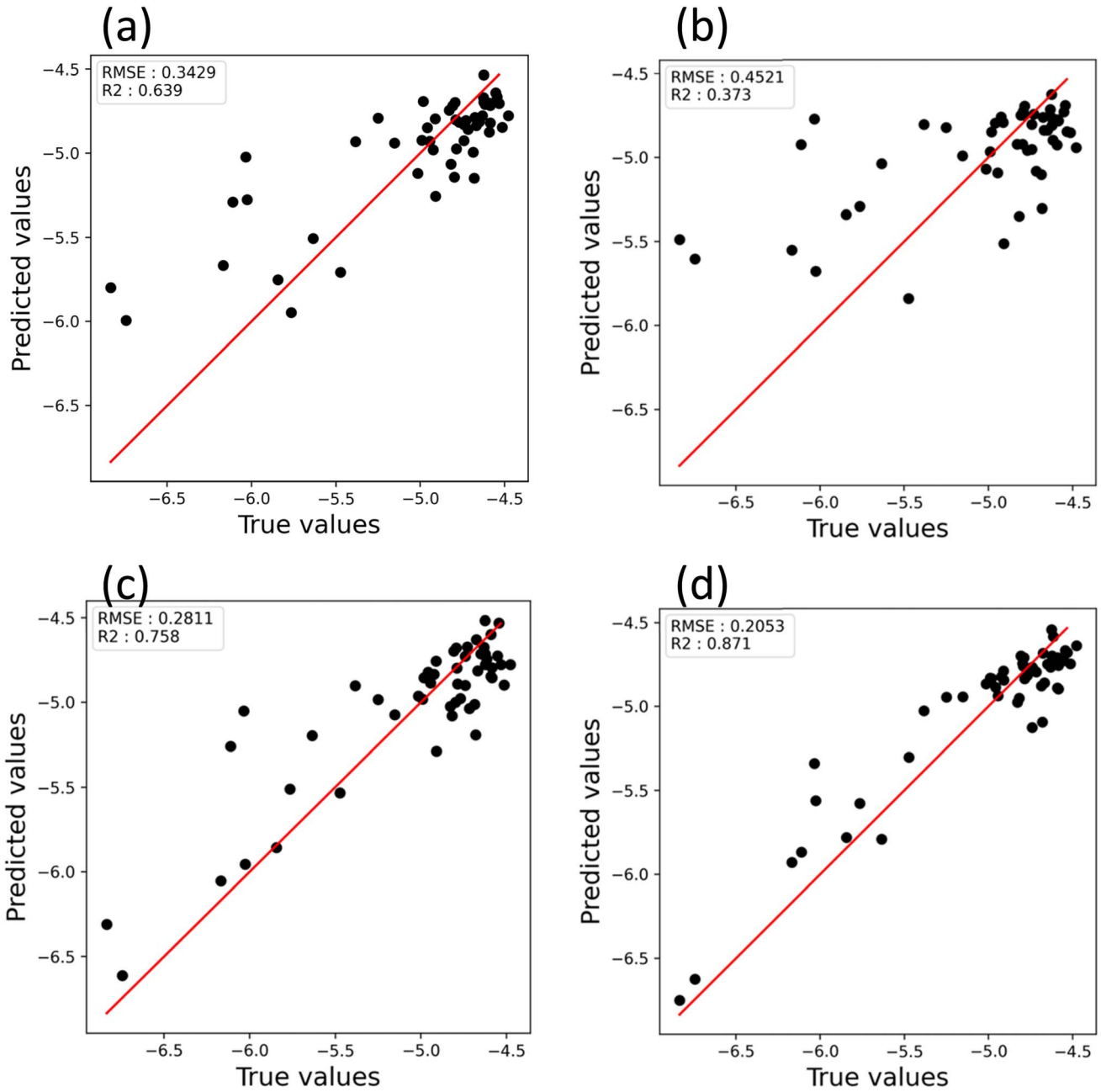

Fig. 3 Diagnostic plots of the logarithmic values of the measured ion conductivity (30 °C) based on SEM images, predicted by (a) the EffcientNet-B3 model, (b) the "Baseline" model, (c) the "Baseline with Attention" model, and (d) the "Baseline with descriptors" model. For each material, one to three SEM images were used for prediction, and the average of these predictions was plotted to represent the sample-level conductivity.

unchanged, a model trained using the "Baseline with Attention" architecture—which incorporates an attention mechanism—was used for test predictions. The resulting diagnostic plot is shown in Fig. 3(c). It was confirmed that the addition of the attention mechanism improved the R^2 score to 0.75. For some materials with low ionic conductivity, the prediction accuracy was significantly improved; however, there still remained outlier samples. This suggests that while SEM images contain information related to ionic conductivity, there is also relevant information that cannot be captured by SEM images alone. Notably, despite being a simpler model without pretrained parameters, the "Baseline" model with attention mechanism achieved results comparable to Efficient Net. This indicates that a relatively simple CNN architecture may be sufficient for SEM image analysis related to ionic conductivity.

To improve the prediction accuracy for images of low ionic conductivity materials—which previously showed lower accuracy—we conducted regression analysis using the "Baseline with descriptors" model, which incorporates additional numerical vector descriptors such as sintering temperatures, composition, and so forth (the specific information of added descriptors is summarized in Table 3). As previously described, material-derived features were newly appended at the GAP layer. The ionic conductivity characteristics of oxide solid electrolytes are

Table 3 A list of the new descriptors added to the GAP layer of "Baseline with descriptors". [X], T1, and T2 correspond to the concentration of element X, the first heating temperature, and the second heating temperature, respectively. All 33 descriptors were standardized before training so that they were input with equal weighting

[Ca]	[Si]	[Li]	[Zr]	[P]	T1	T2
$[Ca]^2$	$[Si]^2$	$[Li]^2$	$[Zr]^2$	$[P]^2$	$T1^2$	$T2^2$
[Ca] × [Si]	[Ca] × [Li]	[Ca] × [Zr]	[Ca] × [P]	[Li] × [Zr]	[Ca] × T1	[Ca] × T2
[Si] × [Li]	[Si] × [Zr]	[Si] × [P]	[Li] × [P]	[Zr] × [P]	[Si] × T1	[Si] × T2
[Li] × T1	[Li] × T2	[Zr] × T1	[Zr] × T2	T1 × T2		

determined by the material composition and the sintering temperature necessary to form ion-conducting pathways. Therefore, in this study, we created 33 descriptors: seven basic descriptors consisting of the molar ratios of [Li, Ca, Zr, Si, P] representing the composition of LCZSP and the first and second sintering temperatures, along with their interaction terms (products). To ensure stable learning within the neural network, these 33 descriptors were standardized to align their scales. Fig. 3(d) shows the diagnostic plots of the "Baseline with descriptors" model. It achieved relatively high prediction accuracy even in the previously challenging low ionic conductivity region, attaining a significant improvement of an R^2 score = 0.871. This indicates that while features such as sintered structure and particle morphology captured in SEM images do contain some information relevant to ionic conductivity, it is essential to also include information not directly visible in SEM images, such as material composition, for accurate prediction of material properties. Although the dataset size (52 samples, 130 images) may appear relatively small compared to typical machine learning benchmarks, it should be noted that in the context of experimental solid electrolyte research this represents a substantial collection effort. Each sample requires careful synthesis, sintering, and characterization, and thus assembling a dataset of this scale is non-trivial. Our results demonstrate that even with such a dataset size, the CNN models are able to achieve reliable predictive performance (R^2 = 0.871), highlighting the practical utility of deep learning approaches for small-data regimes that are common in materials science. Consequently, the "Baseline + descriptors" model was found to be the most accurate among all evaluated models. In addition, we trained a model using only composition- and sintering-related descriptors, without SEM images (SI Fig. S4(a and b)). The resulting R^2 score of 0.38 indicates that such descriptors alone can explain the overall trend but are insufficient for precise predictions. Comparing the three models—(i) descriptors only, (ii) SEM images only, and (iii) descriptors + SEM images—clearly demonstrates that SEM image features provide complementary information to composition and sintering descriptors, leading to the best performance in the combined model. Similar trends were reported by Zhang *et al.*,[37] who used traditional machine learning to correlate microstructural features (grain size, porosity, and grain-boundary fraction) with ionic conductivity in oxide solid electrolytes. Our CNN-based approach builds upon this concept by automatically learning such microstructural features from SEM images while integrating compositional and processing descriptors. To further evaluate the contribution of each descriptor, a feature importance analysis using SHapley Additive exPlanations (SHAP)[50] was conducted. Fig. S4(c) shows the SHAP summary plot for the "descriptors only" model. The results indicate that the first heating temperature (T1) and Si content are the most influential features, followed by their interaction terms (*e.g.*, Si × T1, Zr × T1). These factors are physically meaningful, as excessive Si is known to promote the formation of low-conductivity secondary phases, while a lower first heating temperature reduces sintering density and connectivity of the ion-conducting network. Therefore, the addition of composition- and process-related descriptors to the CNN framework effectively complements the SEM image features and enhances the model's ability to capture the influence of processing and composition on ionic conductivity.

Correlation between SEM images and ionic conductivity

Among the methods for evaluating the interpretability of CNNs, mapping techniques such as Grad-CAM[51] and Score-CAM[52] are widely known. In this study, we adopted the method proposed by Kondo *et al.*[34] to visually assess which features in SEM images contribute to ionic conductivity. This method is only applicable to CNN structures that incorporate Global Average Pooling (GAP). A conceptual diagram of this method is shown in Fig. 4(a).

The GAP layer represents a comprehensive value obtained by learning various features through multiple convolution and pooling layers. Therefore, it can be assumed that the one-dimensional values obtained after GAP have either positive or negative correlations with the ionic conductivity of the input images. By averaging the information in each correlation group, we can visualize their contributions. The visualization process from CNN training is outlined below:

(i) Using the trained CNN model, divide the feature channels into groups that show positive and negative correlations with ionic conductivity.

(ii) For each group, average the feature maps obtained after the final convolution layer (GAP). This means aggregating the information into a single feature map by averaging the pixel values across all channels in the group.

(iii) Since the feature maps generated in (ii) are downsampled compared to the original input image, resize them back to the original image size.

(iv) In the resulting resized feature map, the pixel locations with values higher than the overall median are identified as important regions contributing to ionic conductivity. A masking

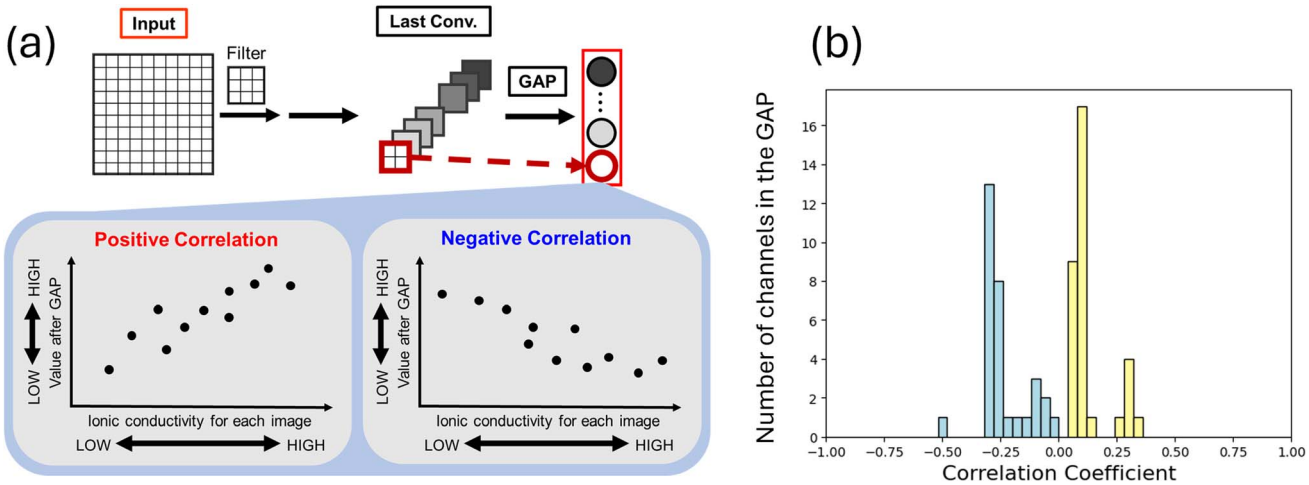

Fig. 4 (a) Schematic image of correlation between each channel and ionic conductivity. (b) A histogram of the correlation coefficients between the GAP feature channels and the ionic conductivity. Yellow and light blue bars correspond to positive and negative correlations, respectively.

operation is then applied to the original SEM image, displaying only these regions.

This series of operations, from (i) to (iv), is referred to as segmentation. In this study, segmentation was performed using the trained "Baseline with descriptors" model, which had achieved the highest regression accuracy, to visualize the relationship between SEM images and ionic conductivity.

Fig. 4(b) shows a histogram of the correlation coefficients between feature channels and ionic conductivity. The model used had 64 channels in its GAP layer. Fig. 4(b) presents a histogram of the correlation coefficients between each channel and ionic conductivity. In our model, the global average pooling (GAP) layer processes 64 channels. As shown in Fig. 4(b), the channel-wise correlation coefficients are relatively low ranging from −0.5 to +0.3. Although the feature maps extracted by the CNN at the GAP layer do not exhibit strong correlations individually, weak inter-channel correlations are present. By aggregating these weak signals, a high overall correlation as shown in Fig. 3 can be derived. Fig. 5 presents segmentation results for four representative materials with high and low ionic conductivity. In the positive examples, it was observed that regions with larger particles were recognized as contributing to high conductivity. Conversely, in the negative examples, grain boundaries were identified as low-conductivity regions. Since grain boundaries

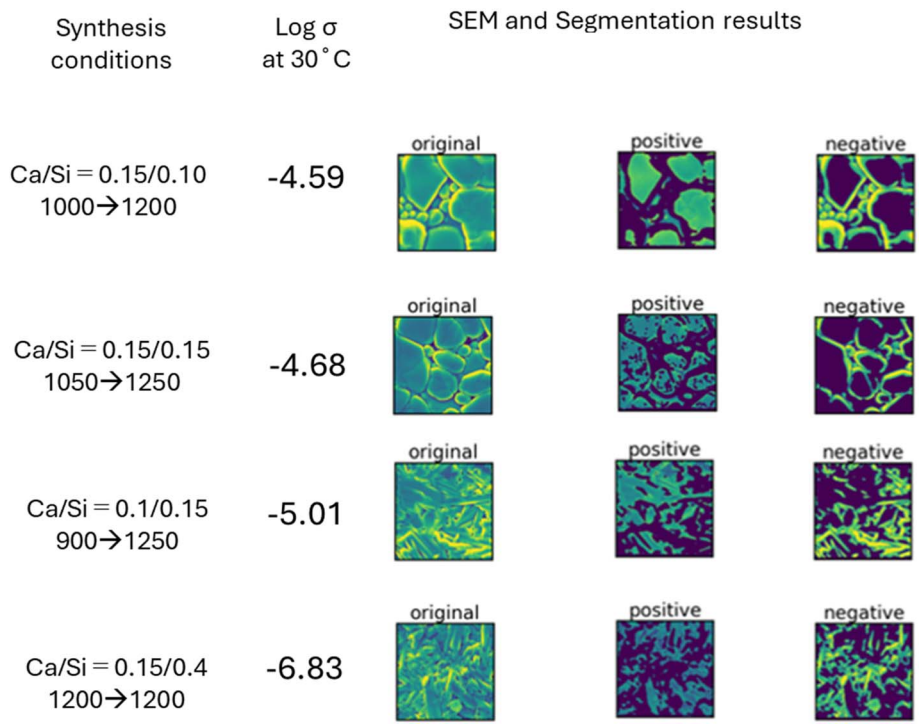

Fig. 5 Excerpts of the segmentation results. Ca/Si and 1st heating/2nd heating represent the molar ratio in the composition and heating temperature (°C), respectively. Segmentation results for the other SEM images are provided in SI datasets.

often disrupt crystal structures, leading to reduced conductivity,[25,53,54] this negative judgment aligns with previous findings. Large, isotropic grains likely represent the bulk of the high-conductivity α-phase and were thus evaluated positively. Notably, channels exhibiting relatively strong negative correlations (*i.e.*, <−0.25) are more prevalent than those with positive correlations (*i.e.*, >+0.25), as shown in Fig. 4(b). This trend suggests increased sensitivity to microstructural features such as grain boundaries and voids observed in the SEM images.

These segmentation results are consistent with established knowledge. However, prior observations have indicated that columnar-like small particles in LZP materials correspond to the low-conductivity β-phase.[25,39] Interestingly, in Fig. 5(c and d), even the bulk of columnar-like crystals—presumed to be β-phase—were evaluated positively, yielding results that differ from known expectations. These results suggest that accurate prediction of ionic conductivity requires the inclusion of composition and structure information. In our "Baseline + descriptors" model, explicitly providing composition and sintering-temperature data enabled us to incorporate details about the resulting α- and β-phases.

Nonetheless, this method demonstrates the ability to extract valuable insights regarding material microstructures related to ionic conductivity directly from SEM images. Typically, interpreting SEM images requires expert knowledge and experience in materials research, but segmentation can help reduce the effort required for such analyses and improve efficiency.

Conclusion

In this study, we used various CNN architectures to predict the ionic conductivity of LCZSP materials based on SEM images that contain complex structural information. Although SEM images are manually acquired and thus difficult to obtain in large quantities, we demonstrated that with appropriate CNN architecture design, high prediction accuracy can be achieved even with a limited dataset of only 130 images. The "Baseline + descriptors" model, which incorporates both compositional and sintering condition information into the SEM image analysis, achieved a high R^2 score of 0.871. The ability to integrate synthesis conditions into the model is a key advantage of leveraging raw data. By combining this with intuitive information from SEM images, a more powerful predictive model can be realized. Furthermore, we explored the interpretability of the trained models by performing segmentation based on the correlation between GAP layer channels and ionic conductivity. By categorizing the channels into positively and negatively correlated groups, we were able to clearly distinguish high-conductivity and low-conductivity regions within SEM images. The results showed that the presence of large particles tends to correspond with higher ionic conductivity, whereas the presence of small particles or grain boundaries is associated with lower conductivity. This indicates that interfacial regions between particles play a critical role in the ionic conductivity of solid electrolytes. Interestingly, even relatively simple convolutional-only architectures yielded good segmentation results, suggesting that complex operations are not necessarily required to capture material features effectively. In fact, excessive convolutional stacking may obscure the original pixel-level location information, potentially impairing accurate interpretation. Moreover, while SEM image data alone cannot fully characterize the ionic conductivity of solid electrolytes, we found that incorporating information such as composition and sintering temperature into the GAP layer compensates for this deficiency.

Furthermore, transfer learning represents a promising future direction. Our preliminary tests with EfficientNet-B3 pretrained on ImageNet already improved baseline accuracy, suggesting that the availability of larger SEM datasets will further enhance generalizability and emphasize the importance of open data initiatives. This methodology is not only applicable to the LCZSP materials studied here but can also be extended to other systems, enabling the effective utilization of routinely acquired SEM images.

Author contributions

H. T. and M. N. conceived and designed the study. K. M. and H. T. performed SEM imagings and data curation. K. M. and Y. Y. coded and analyzed data by the deep learning technique with the help of M. K. The manuscript was written mainly by K. M., H. T. and M. N. through contributions from all authors. All the authors have approved the final version of the manuscript.

Conflicts of interest

There are no conflicts of interest.

Data availability

Datasets (SEM images and descriptor table) are available in Figshare: https://doi.org/10.6084/m9.figshare.28944998.

Supplementary information: conditions of neural network settings. See DOI: https://doi.org/10.1039/d5dd00232j.

Acknowledgements

A part of this study was based on results supported by the following projects: a Grants-in-Aid for Scientific Research (Grant No. 24H02203, and 24K01157) from the Ministry of Education, Culture, Sports, Science, and Technology (MEXT), Japan; a CREST grant from the Japan Science and Technology Agency, Japan (Grant No. JPMJCR21O6), and the Data Creation and Utilization Type Material Research and Development Project (Grant No. JPMXP1122712807) of MEXT.

References

1 K. Takada, *Acta Mater.*, 2013, **61**, 759–770.
2 F. Zheng, M. Kotobuki, S. Song, M. O. Lai and L. Lu, *J. Power Sources*, 2018, **389**, 198–213.
3 Y. Zheng, Y. Yao, J. Ou, M. Li, D. Luo, H. Dou, Z. Li, K. Amine, A. Yu and Z. Chen, *Chem. Soc. Rev.*, 2020, **49**, 8790–8839.
4 J. Sung, J. Heo, D.-H. Kim, S. Jo, Y.-C. Ha, D. Kim, S. Ahn and J.-W. Park, *Mater. Chem. Front.*, 2024, **8**, 1861–1887.

5 J. Janek and W. G. Zeier, *Nat. Energy*, 2023, **8**, 230–240.
6 B. Liu, J.-G. Zhang and W. Xu, *Joule*, 2018, **2**, 833–845.
7 Y. Inaguma, C. Liquan, M. Itoh, T. Nakamura, T. Uchida, H. Ikuta and M. Wakihara, *Solid State Commun.*, 1993, **86**, 689–693.
8 R. Murugan, V. Thangadurai and W. Weppner, *Angew. Chem., Int. Ed.*, 2007, **46**, 7778–7781.
9 M. Kotobuki and M. Koishi, *J. Asian Ceram. Soc.*, 2019, **7**, 551–557.
10 H. Aono, E. Sugimoto, Y. Sadaoka, N. Imanaka and G. ya Adachi, *Solid State Ionics*, 1990, **40–41**, 38–42.
11 J. B. Goodenough, H. Y.-P. Hong and J. A. Kafalas, *Mater. Res. Bull.*, 1976, **11**, 203–220.
12 W. Xia, B. Xu, H. Duan, Y. Guo, H. Kang, H. Li and H. Liu, *ACS Appl. Mater. Interfaces*, 2016, **8**, 5335–5342.
13 Y. Li, W. Zhou, X. Chen, X. Lü, Z. Cui, S. Xin, L. Xue, Q. Jia and J. B. Goodenough, *Proc. Natl. Acad. Sci. U. S. A.*, 2016, **113**, 13313–13317.
14 S. Kumar and P. Balaya, *Solid State Ionics*, 2016, **296**, 1–6.
15 S. Smith, T. Thompson, J. Sakamoto, J. L. Allen, D. R. Baker and J. Wolfenstine, *Solid State Ionics*, 2017, **300**, 38–45.
16 E. R. Losilla, M. A. G. Aranda, M. Martínez-Lara and S. Bruque, *Chem. Mater.*, 1997, **9**, 1678–1685.
17 H. Xie, Y. Li and J. B. Goodenough, *RSC Adv.*, 2011, **1**, 1728.
18 A. Cassel, B. Fleutot, M. Courty, V. Viallet and M. Morcrette, *Solid State Ionics*, 2017, **309**, 63–70.
19 Y. Li, M. Liu, K. Liu and C.-A. Wang, *J. Power Sources*, 2013, **240**, 50–53.
20 M. F. Zawrah and L. Shaw, *Ceram. Int.*, 2004, **30**, 721–725.
21 Y. Zhang, K. Chen, Y. Shen, Y. Lin and C.-W. Nan, *Ceram. Int.*, 2017, **43**, S598–S602.
22 V. I. Pet'kov, M. V Sukhanov, A. S. Shipilov, V. S. Kurazhkovskaya, E. Yu. Borovikova, I. Yu Pinus and A. B. Yaroslavtsev, *Inorg. Mater.*, 2014, **50**, 263–272.
23 D. Safanama and S. Adams, *J. Power Sources*, 2017, **340**, 294–301.
24 X. Xu, Z. Wen, X. Wu, X. Yang and Z. Gu, *J. Am. Ceram. Soc.*, 2007, **90**, 2802–2806.
25 M. Nakayama, K. Nakano, M. Harada, N. Tanibata, H. Takeda, Y. Noda, R. Kobayashi, M. Karasuyama, I. Takeuchi and M. Kotobuki, *Chem. Commun.*, 2022, **58**, 9328–9340.
26 H. Takeda, H. Fukuda, K. Nakano, S. Hashimura, N. Tanibata, M. Nakayama, Y. Ono and T. Natori, *Mater. Adv.*, 2022, **3**, 8141–8148.
27 M. Harada, H. Takeda, S. Suzuki, K. Nakano, N. Tanibata, M. Nakayama, M. Karasuyama and I. Takeuchi, *J. Mater. Chem. A*, 2020, 15103–15109.
28 H. Fukuda, S. Kusakawa, K. Nakano, N. Tanibata, H. Takeda, M. Nakayama, M. Karasuyama, I. Takeuchi, T. Natori and Y. Ono, *RSC Adv.*, 2022, **12**, 30696–30703.
29 H. Takeda, K. Murakami, Y. Yamaguchi, H. Fukuda, N. Tanibata, M. Nakayama, T. Natori, Y. Ono and N. Saito, *Next Mater.*, 2025, **8**, 100574.
30 K. Rajan, *Mater. Today*, 2005, **8**, 38–45.
31 C. Chen, Y. Zuo, W. Ye, X. Li, Z. Deng and S. P. Ong, *Adv. Energy Mater.*, 2020, **10**, 1903242.
32 M. Nakayama, *J. Ceram. Soc. Jpn.*, 2021, **129**, 286–291.
33 Y. Yokoyama, S. Noguchi, K. Ishikawa, N. Tanibata, H. Takeda, M. Nakayama, R. Kobayashi and M. Karasuyama, *APL Mater.*, 2024, **12**, 111120.
34 R. Kondo, S. Yamakawa, Y. Masuoka, S. Tajima and R. Asahi, *Acta Mater.*, 2017, **141**, 29–38.
35 K. Simonyan and A. Zisserman, *arXiv*, 2015, preprint, arXiv:1409.1556v6, DOI: 10.48550/arXiv.1409.1556.
36 R. Furushima, Y. Nakashima, Y. Maruyama, Y. Zhou, K. Hirao, T. Ohji and M. Fukushima, *J. Am. Ceram. Soc.*, 2025, **108**, e20173.
37 Y. Zhang, X. Lin, W. Zhai, Y. Shen, S. Chen, Y. Zhang, Y. Yu, X. He and W. Liu, *Nano Lett.*, 2024, **24**, 5292–5300.
38 K. Murakami, Y. Kato, H. Takeda and M. Nakayama, *Figshare*, 2025, DOI: 10.6084/m9.figshare.28944998.
39 H. Xu, S. Wang, H. Wilson, F. Zhao and A. Manthiram, *Chem. Mater.*, 2017, **29**, 7206–7212.
40 M. Tan and Q. V. Le, *arXiv*, 2020, preprint, arXiv:1905.11946v5, DOI: 10.48550/arXiv.1905.11946.
41 K. Yang, K. Qinami, L. Fei-Fei, J. Deng and O. Russakovsky, in *Proceedings of the 2020 Conference on Fairness, Accountability, and Transparency*, Association for Computing Machinery, New York, NY, USA, 2020, pp. 547–558.
42 H. Fukui, T. Hirakawa, T. Yamashita and H. Fujiyoshi, *arXiv*, 2018, preprint, arXiv:1812.10025, DOI: 10.48550/arXiv.1812.10025.
43 J. Hu, L. Shen and G. Sun, in *2018 IEEE/CVF Conference on Computer Vision and Pattern Recognition*, 2018, pp. 7132–7141.
44 F. Wang, M. Jiang, C. Qian, S. Yang, C. Li, H. Zhang, X. Wang and X. Tang, in *2017 IEEE Conference on Computer Vision and Pattern Recognition (CVPR)*, 2017, pp. 6450–6458.
45 M. Lin, Q. Chen and S. Yan, *arXiv*, 2014, preprint, arXiv:1312.4400v3, DOI: 10.48550/arXiv.1312.4400.
46 C. Szegedy, W. Liu, Y. Jia, P. Sermanet, S. Reed, D. Anguelov, D. Erhan, V. Vanhoucke and A. Rabinovich, in *2015 IEEE Conference on Computer Vision and Pattern Recognition (CVPR)*, 2015, pp. 1–9.
47 K. He, X. Zhang, S. Ren and J. Sun, *arXiv*, 2015, preprint, arXiv:1512.03385v1, DOI: 10.48550/arXiv.1512.03385.
48 J. Long, E. Shelhamer and T. Darrell, *arXiv*, 2014, preprint, arXiv:1411.4038, DOI: 10.48550/arXiv.1411.4038.
49 K. Murakami, Y. Kato, H. Takeda and M. Nakayama, *Figshare*, 2025, DOI: 10.6084/m9.figshare.28944998.
50 S. M. Lundberg, G. G. Erion and S.-I. Lee, *arXiv*, 2019, preprint, arXiv:1802.03888v3, DOI: 10.48550/arXiv.1802.03888.
51 R. R. Selvaraju, M. Cogswell, A. Das, R. Vedantam, D. Parikh and D. Batra, *Int. J. Comput. Vis.*, 2020, **128**, 336–359.
52 H. Wang, M. Du, F. Yang and Z. Zhang, *ArXiv*, 2019, preprint, pp. 1–11.
53 H. Shiiba, N. Zettsu, M. Yamashita, H. Onodera, R. Jalem, M. Nakayama and K. Teshima, *J. Phys. Chem. C*, 2018, **122**, 21755–21762.
54 K. Nakano, N. Tanibata, H. Takeda, R. Kobayashi, M. Nakayama and N. Watanabe, *J. Phys. Chem. C*, 2021, **125**, 23604–23612.